MMP-7 promotes prostate cancer-induced osteolysis via the solubilization of RANKL

Conor C. Lynch,[1] Atsuya Hikosaka,[3,4] Heath B. Acuff,[1] Michelle D. Martin,[1] Noriyasu Kawai,[4] Rakesh K. Singh,[5] Tracy C. Vargo-Gogola,[1] Jennifer L. Begtrup,[2] Todd E. Peterson,[2] Barbara Fingleton,[1] Tomoyuki Shirai,[3] Lynn M. Matrisian,[1] and Mitsuru Futakuchi[3,5,*]

[1]Department of Cancer Biology, Vanderbilt University, 23rd and Pierce Avenue, Nashville, Tennessee, 37232
[2]VUIIS, Vanderbilt University, 23rd and Pierce Avenue, Nashville, Tennessee, 37232
[3]Department of Experimental Pathology and Tumor Biology, Nagoya City University Medical School, Nagoya 467-8601, Japan
[4]Department of Nephro-Urology, Nagoya City University Medical School, Nagoya 467-8601, Japan
[5]Department of Pathology and Microbiology, University of Nebraska Medical Center, 985845 Nebraska Medical Center, Omaha, Nebraska, 68198
*Correspondence: mfutakuchi@unmc.edu

Summary

We developed a rodent model that mimics the osteoblastic and osteolytic changes associated with human metastatic prostate cancer. Microarray analysis identified *MMP-7*, *cathepsin-K*, and *apolipoprotein D* as being upregulated at the tumor-bone interface. MMP-7, which was produced by osteoclasts at the tumor-bone interface, was capable of processing RANKL to a soluble form that promoted osteoclast activation. MMP-7-deficient mice demonstrated reduced prostate tumor-induced osteolysis and RANKL processing. This study suggests that inhibition of MMP-7 will have therapeutic benefit in the treatment of prostate cancer-induced osteolysis.

Introduction

In the United States alone, 29,900 deaths from prostate cancer were expected in 2004 (American Cancer Society, 2004). These deaths are primarily due to metastases that are resistant to conventional therapies. The most common site for metastasis of prostate cancer is the bone, with patients often experiencing intense pain, pathological fracture, hypercalcemia, and immobility (see [Mundy, 2002] for review). Currently, there are few successful treatment options for patients with bone metastases that can improve overall patient survival (Chay et al., 2002). To address this and to identify new therapeutic targets, the molecular mechanisms underlying prostate tumor induced changes in the bone microenvironment need to be elucidated. However, one of the major drawbacks in identifying these mechanisms is the lack of animal models that mimic the manifestation of human prostate carcinoma skeletal metastasis.

Human bone metastases of prostate cancer are mixed lesions, typically containing regions of invading tumor coupled with areas of osteoblastic and osteolytic change (Keller and Brown, 2004). Unfortunately, current metastatic prostate cancer animal models and cell lines lack these histological features of clinical prostate cancers metastases or produce low rates of metastasis to bone (Shevrin et al., 1989; Nemeth et al., 1999; Zhau et al., 2000; Corey et al., 2002). Therefore, it is difficult to address the full complement of molecular interactions at work in the metastatic prostate cancer bone microenvironment using these models.

Our current understanding of how metastatic prostate cancer cells induce osteoblastic lesions is poor, although several studies have shown transforming growth factor β (TGF-β) to play an important role in the stimulation of osteoblast proliferation and bone matrix formation (Keller and Brown, 2004). On the contrary, more is known about osteolytic lesions induced by the tumor cells. The interaction between the tumor and bone stroma has been commonly referred to as the "vicious cycle," whereby tumor cells in the bone can secrete factors such as parathyroid hormone related peptide (PTHrP) that stimulate osteoblast expression of the TNF family member *r*eceptor *a*ctivator of *n*uclear κB *l*igand (RANKL). By binding to the receptor RANK, RANKL has been shown to be essential in mediating osteoclast activation. The osteoclasts degrade the bone matrix using a powerful array of proteinases such as the cathepsins and matrix metalloproteinases (MMPs) (see [De-

SIGNIFICANCE

Understanding how metastatic prostate cancer cells induce changes in bone matrix homeostasis is essential for the identification of new therapies to control metastatic disease. Here, we describe an in vivo model that accurately recapitulates the behavior of human metastatic prostate cancer in the bone environment by developing mixed osteoblastic and osteolytic lesions. Using this model, we identified the expression of MMP-7 at the tumor-bone interface and demonstrated a molecular mechanism by which MMP-7 can mediate osteolysis. Our study contributes to the growing consensus for the use of MMP inhibitors for the treatment of pathological bone disease.

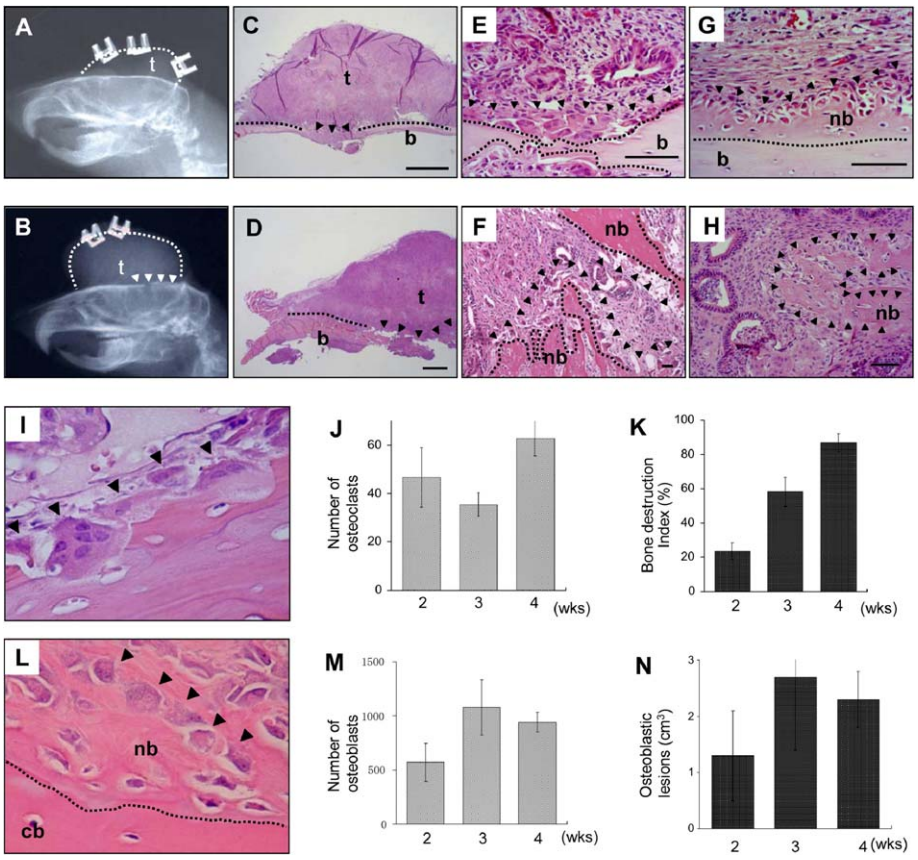

Figure 1. Model of prostate cancer-induced osteolytic and osteoblastic change

A: Postoperative X-ray analysis of the tumor (t). Note intact calvaria.

B: At week 4, areas of osteolysis could be discerned by X-ray (arrows), and the tumor volume also increased (dashed line represents tumor border).

C–D: Coronal sections of the cranial bone stained with H&E at weeks 2 and 4, respectively (black dashed line represents intact calvaria; arrows indicate areas of osteolysis; b denotes bone; scale bars represent 2 mm).

E: Higher magnification of the H&E-stained samples demonstrated the presence of multinucleated osteoclasts lining the TB interface at week 2. Arrows indicate osteoclasts; scale bar is 0.1 mm.

F: H&E-stained sections at week 4. Note that more osteoclasts were observed. Scale bar represents 0.5 mm.

G: H&E stained sections of areas of osteoblastic change at week 2. Arrows indicate osteoblasts; nb represents new bone formation; scale bar represents 0.02 mm.

H: H&E-stained sections at week 4 with pronounced areas of osteoblastic change (arrows indicate osteoblasts). Scale bar represents 0.5 mm.

I: H&E-stained section of the TB interface at week 4. Osteoclasts are indicated by arrows.

J: Mean ± SD of the number of osteoclasts at weeks 2, 3, and 4 (n = 3 for each time point).

K: Bone destruction index is calculated as percent of bone underneath the tumor demonstrating osteolysis (n = 3 for each time point). Values are mean ± SD.

L: H&E-stained section at week 4. Arrows indicate osteoblasts (nb, new bone; cb, calvarial bone).

M: Mean ± SD of the number of osteoblasts at weeks 2, 3, and 4 (n = 3 for each time point).

N: Mean ± SD of the area of new bone per coronal section (n = 3 for each time point). Amount of new bone area formed by the osteoblasts was also quantified.

Error bars represent standard deviation.

laisse et al., 2003] for review). Degradation of the bone matrix leads to the release of TGF-β and other growth factors that in turn stimulate tumor growth and lead to increased levels of tumor derived PTHrP (see [Mundy, 2002] for review).

These factors outlined above contribute to our understanding of how prostate tumor cells can potentially induce changes in the bone. However, it is likely that there are many more unidentified factors present in the tumor-bone microenvironment that dictate how the bone stroma will respond to the metastatic tumor cells, and vice versa. The aim of the current study was to generate an animal model that accurately reflects the behavior of human prostate cancer in the bone with respect to the induced changes in bone matrix homeostasis, and to identify the molecules that underlie the behavior of this disease.

Results

Establishment of a rat model of human prostate cancer in the bone

To mimic the metastatic human prostate bone environment, pieces of moderately differentiated prostate adenocarcinoma, generated in rats as previously described (Kato et al., 1998), were transplanted into the cranial region of syngeneic animals. At early time points, little or no change in the bone density of the calvaria was observed by X-ray radiography (Figure 1A). However, clear osteolytic lesions were visually identified in the calvaria at week 4 (Figure 1B). Histopathological analysis of the tumor-bone interface (TB interface) revealed both osteolytic and osteoblastic changes over the course of the experiment (Figures 1C and 1D). Inspection of the TB interface demonstrated small bone defects and the presence of osteoclasts at week 2 (Figure 1E). At week 4, osteoclasts were observed at the TB interface, and a larger area of bone absorption in comparison to week 2 was noted (Figure 1F). Small areas of nodular osteoid produced by the osteoblasts were also identified at week 2, and these areas increased through week 4 (Figures 1G and 1H).

Under high magnification, it was clear that the osteoclast cells were responsible for the tumor-induced osteolysis at the TB interface, as they separated the prostate tumor cells from the bone matrix (Figure 1I). We determined the number of osteoclasts present at each experimental time point in order to examine the effects of the prostate tumor on osteoclast recruitment and activity. Several coronal sections from each rat were examined, and approximately fifty osteoclasts per section were found to accumulate at the TB interface by week 2 (Figure 1J). These levels remained elevated at the 3- and 4-week time points. In comparison, no osteoclasts were recruited to the site of sham operations in the control animals at days 0 or 14 (data

not shown). We also examined the extent of bone destruction in several sections from each rat using a "bone destruction index," which refers to the length of osteolysis per length of cranial bone beneath the transplanted tumors. We found that the bone destruction index was on average 30% at week 2, and that the extent of destruction increased up to 90% at week 4 (Figure 1K). The number of osteoclasts at each time point did not correlate with the extent of bone destruction, suggesting that the prostate tumor cells recruit the osteoclasts rapidly to the TB interface, and induce osteolytic lesions gradually.

Our rat model also displayed large areas of osteoblast activity and nodular-osteoid formation. These osteoid formations, because of their amorphous structure, were easily identified in comparison to the laminar bone of the calvaria (Figure 1L). We counted the osteoblasts present at the TB interface in several coronal sections from each rat and found that the numbers increased from approximately 500 at week 2 to 1000 at weeks 3 and 4 (Figure 1M). We measured the tumor-induced osteoid formations and found that they increased at all time points, which correlated to the number of osteoblasts (Figure 1N).

We also generated a spinal implant model, representing cartilagenous rather than membraneous bone, and our findings were similar to those described for the cranial model (data not shown). No osteoblastic or osteolytic changes were observed when sham surgeries were performed on control rats in either the cranial or spinal models (data not shown).

Importantly, the histological observations at the TB interface in our animal model mimic the histological features of metastatic bone lesions in human prostate cancers. The model therefore presents an exciting opportunity to examine the molecular mechanisms underlying how tumor cells can induce osteoblastic and osteolytic changes in the bone lesions.

Expression of PTHrP, RANKL, and OPG at the TB interface

We next characterized the expression of molecules known to be important for pathological changes in the bone environment, including PTHrP, RANKL, and osteoprotegerin (OPG) (Mundy, 2002). Using quantitative real-time PCR, we compared the mRNA expression of these molecules at the TB interface to the tumor area alone (Figure 2A). The TB interface was comprised of tumor cells invading into the bone, osteoblasts inducing osteoid formation, and osteoclasts mediating osteolysis, while the tumor area was primarily comprised of prostate tumor cells with occasional stromal elements (Figures 2B and 2C).

PTHrP in the bone environment is an important regulator of osteoblast function. *PTHrP* was constantly expressed in the tumor area alone over the course of the experiment, although the levels tended toward a decrease with time (Figure 2D). In comparison, the levels of *PTHrP* were much higher at the TB interface over the course of the experiment. These observations are consistent with the "vicious cycle" concept whereby bone-derived factors stimulate tumor PTHrP expression. PTHrP stimulates the expression of RANKL by osteoblasts and is essential in mediating osteoclast activation (Mundy, 2002). In our model, *RANKL* was expressed at a significantly higher level at the TB interface compared to the tumor alone at each experimental time point (Figure 2E). The effects of RANKL can be inhibited by the binding of a soluble decoy receptor molecule, OPG (Simonet et al., 1997). Real-time PCR analysis of OPG expression demonstrated that there was a significantly higher level of *OPG* expression at the TB interface at week 2 in comparison to the tumor area alone (Figure 3F). However, at the 3- and 4-week time points, a significant decrease in *OPG* expression was observed at the TB interface. This decrease in *OPG* over time, in contrast to the persistently high levels of *RANKL* and *PTHrP*, is consistent with the observed increases in osteoclast activation and bone destruction occurring at the TB interface.

Several reports have recently suggested that RANKL is also expressed by the prostate tumor cells (Brown et al., 2001). Although we observed *RANKL* mRNA expression in the tumor area alone (Figure 2E), immunohistochemical staining for RANKL demonstrated that the osteoblasts were the main source of RANKL in our model (Figure 2G), as little or no staining was observed in the osteoclasts or in the tumor cells (Figures 2H and 2I).

Gene expression at the TB interface

Having demonstrated that the rat model was recapitulating the histological features of metastatic human prostate cancer in the bone, we used microarray analysis to examine the expression of 1200 genes at the TB interface and tumor areas from both the cranial and spinal models at the 4-week experimental time point. Several genes showed significant elevation at the TB interface in both models, including *apolipoprotein-D* (*Apo-D*), *matrix metalloproteinase-7* (*MMP-7*), and *cathepsin-K* (*Cat-K*) (Figure 3A). Genes that were significantly decreased included *adenine nucleotide translocator 2* (*ANT2*), *ATPase*, *Ca^{2+} transporting*, *cardiac muscle* (*BCAT*), *aquaporin-8* (*AQP-8*), and *channel-inducing factor* (*CHIF*). The presence of genes that are differentially expressed in both the cranial and spinal models suggested common mechanisms of osteolysis that are independent of intramembraneous or intracartilaginous ossification.

Real-time PCR was used to validate the expression of candidate genes identified by microarray analysis. We also assessed the sequential expression of these genes at the TB interface and tumor areas in order to determine if there was a correlation with osteolytic and/or osteoblastic changes. Apo-D is a member of the lipocalcin family of hydrophobic protein transporters. We found that the expression of *Apo-D* gradually increased over time and was significantly higher at the TB interface in comparison to the tumor area at all time points (Figure 3B). The exact role of Apo-D in prostate tumor progression remains unclear; however, it may be involved in the growth and development of hormone-responsive tissue because of an ability to bind hormones such as progesterone (Rassart et al., 2000).

Significantly higher mRNA levels of *MMP-7* were found at the TB interface in comparison to the tumor area alone. Interestingly, *MMP-7* expression showed a good correlation with the bone destruction index (Figure 1K). MMP-7 is one of the smallest members of the MMP family and is capable of hydrolyzing a vast array of extracellular matrix (ECM) and non-ECM derived substrates (see [Lynch and Matrisian, 2002] for review). However, no role for MMP-7 in the pathological bone environment has been described.

Cat-K, a powerful cysteine proteinase produced by osteoclasts, has an important role in bone matrix turnover (Gowen et al., 1999), and the mRNA expression levels at the TB interface correlated with the number of osteoclasts (Figures 1J and 3D). Little *Cat-K* expression was observed in the tumor area. The

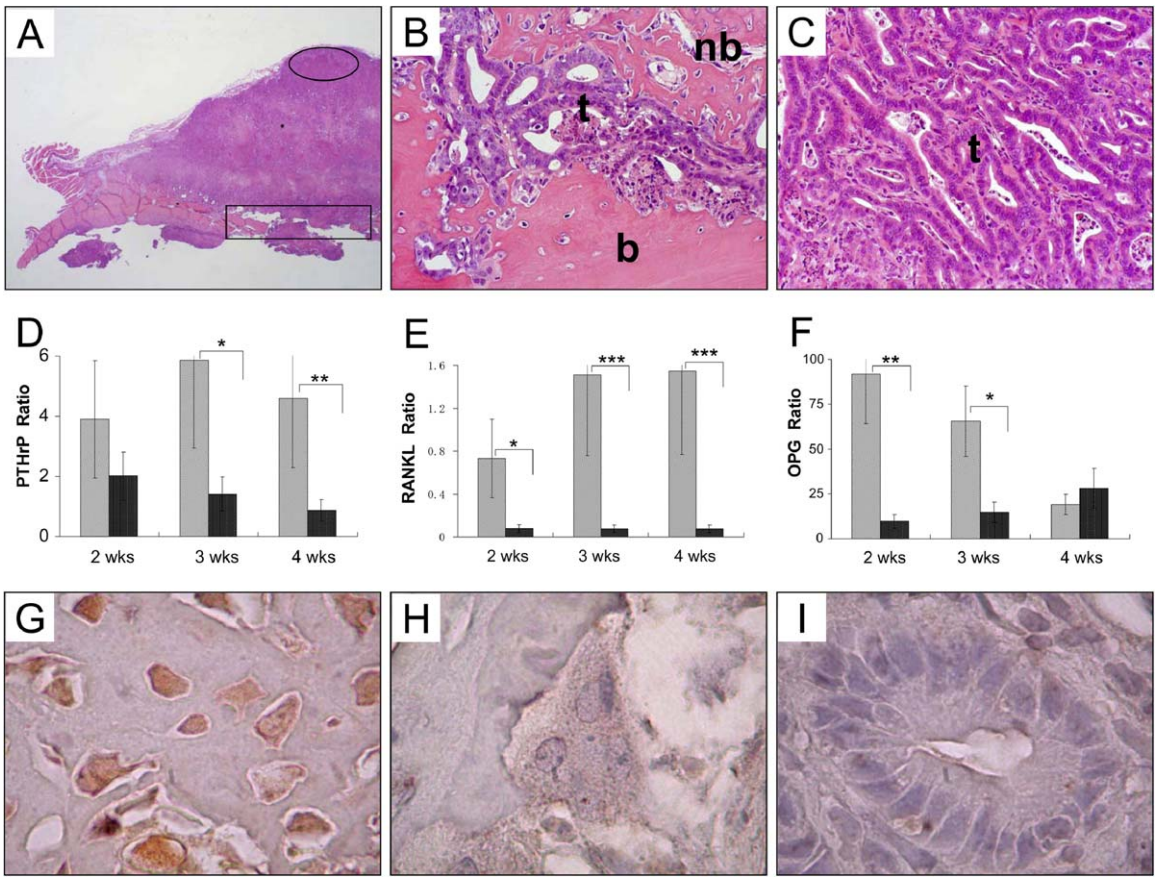

Figure 2. Characterization of the rat prostate bone invasion model

A: For mRNA analysis, the samples were divided into areas of TB interface (rectangle) and tumor area alone (oval).

B: H&E-stained section of the TB interface comprised of areas of tumor (t), bone (b), and new bone (nb).

C: H&E-stained section of the tumor area comprised primarily of tumor cells (t).

D–F: Real-time PCR analysis of *PTHrP, RANKL*, and *OPG* gene expression over time was performed on three rats from each experimental time point. Striped bars represent values obtained from the tumor bone interface, while solid bars represent the values obtained from the tumor area alone. To obtain the ratios, target gene expression was normalized to *GAPDH*. *, $p < 0.05$; **, $p < 0.01$; ***, $p < 0.001$.

G–I: Immunohistochemical staining for RANKL in the osteoblasts (**G**) osteoclasts (**H**) and tumor cells (**I**) at week 4. Multiple sections from each time point were examined with similar results.

Error bars represent standard deviation.

identification of Cat-K at the TB interface demonstrated that the microarray data obtained was consistent with previously published reports on the role of this proteinase in osteolysis.

Several genes were also significantly decreased at the TB interface in comparison to the tumor area alone. Upon analysis with real-time PCR, no significant differences between the TB interface and the tumor were observed at any experimental time point for *ANT-2*, *BCAT*, and *CHIF* (data not shown). The expression of *AQP-8*, a member of the transmembrane water channel aquaporins (Koyama et al., 1997), also showed no difference at weeks 2 to 3, but a significant reduction in the expression of *AQP-8* at the TB interface compared to the tumor alone was noted at week 4 (Figure 3E).

MMP-7 is expressed by osteoclasts in vivo and in vitro

A number of studies have shown that the MMPs are important in bone matrix development and homeostasis and that broad-spectrum MMP inhibitors (MMPIs) are efficient in the prevention of osteolysis (see [Delaisse et al., 2003] for review). The identification and validation of *MMP-7* mRNA at the TB interface coupled to the promise of MMPIs in the treatment of osteolysis led us investigate the role of MMP-7 at the TB interface. Immunohistochemical analysis revealed that cells resembling osteoclasts, present at the TB interface at week 4, were positive for MMP-7 (Figures 4A and 4B). To confirm that the cells expressing MMP-7 were osteoclasts, we used the histochemical marker for activated osteoclasts, tartrate-resistant acid phosphatase (TRAP), in adjacent serial tumor sections (Figures 4C and 4D). We also observed that MMP-7 was not expressed by the prostate tumor cells or in areas where osteoblastic changes were occurring, thereby suggesting that the role of MMP-7 was connected to prostate cancer-induced osteolysis (Figures 4E and 4F). To corroborate evidence that osteoclasts can express MMP-7, we examined an immortalized osteoclast cell line (Hentunen et al., 1999). RT-PCR and immunoblot analysis confirmed the expression of MMP-7 in these

A

Genes up- or downregulated in TB interface	TB interface / Tumor area	
	Skull	Spine
Upregulated		
Apolipoprotein D	15.61	19.11
Matrix metalloproteinase 7 (matrilysin, MMP7)	9.25	4.52
Cathepsin K	7.13	2.55
Downregulated		
Fibroblast ADP/ATP carrier protein; ADP/ATP translocase 2; adenine nucleotide translocator 2 (ANT2)	0.07	0.06
ATPase, Ca2+ transporting, cardiac muscle (BCAT)	0.14	0.34
Aquaporin 8 (AQP 8)	0.19	0.22
Channel-inducing factor; corticosteroid-induced protein (CHIF)	0.24	0.43

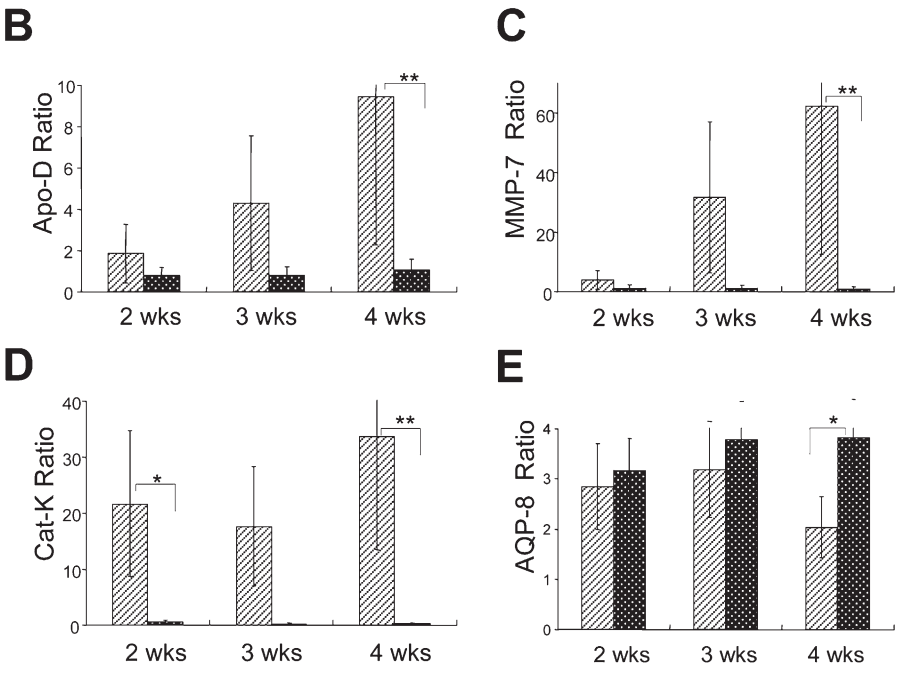

Figure 3. Identification of differentially expressed genes at the TB interface

A: Comparative microarray analysis of genes expressed at the TB interface and the tumor area. The upregulated values represent the fold increase in expression of a particular gene at the TB interface when compared to the tumor alone, and the downregulated values represent the inverse reciprocal fold decrease in expression of candidate genes at the TB interface when compared to the tumor alone.

B–E: *Apo-D*, *MMP-7*, *Cat-K*, and *AQP-8*: *GAPDH* mRNA ratio at the tumor bone interface (striped bars) and tumor area alone (solid bars). *, $p < 0.05$; **, $p < 0.01$ ($n = 3$ for each experimental time point).

Error bars represent standard deviation.

cells (Figures 4G and 4H). Collectively, these data demonstrate that MMP-7 is expressed both in vivo and in vitro by osteoclasts.

MMP-7 cleaves RANKL to a soluble active form

We hypothesized that osteoclast MMP-7 expression was linked to osteolysis based on the positive correlation between MMP-7 expression and bone destruction (Figures 1K and 3C). Given that MMP-7 has a broad extracellular matrix (ECM) substrate specificity, an obvious role for MMP-7 expression by the osteoclasts would be in the degradation of bone matrix. However, MMP-7 has often been associated with "sheddase" activity rather than bulk degeneration of the ECM. In this regard, MMP-7 has been shown to convert membrane-bound forms of TNF family members such as TNF and FasL to soluble active forms (see [Lynch and Matrisian, 2002] for review). Interestingly, the levels of the TNF family member RANKL also correlated with the extent of bone destruction in our model (Figures 1K and 2E). In addition, RANKL contains putative metalloproteinase cleavage sites (Nakashima et al., 2000), and transgenic animals expressing a soluble version of RANKL exhibit extensive osteoporosis (Mizuno et al., 2002). We therefore hypothesized that the potential mechanism through which MMP-7 may be promoting osteolysis was via the solubilization of RANKL, which is an essential mediator of osteoclast activation.

To determine if MMP-7 was capable of cleaving RANKL, full-length RANKL protein was generated using an in vitro translation system. Analysis of translation products generated from the RANKL expression vector demonstrated the predicted full-length unglycosylated 38 kDa product (Figure 5A, control lane). After 6 hr incubation, enzymatically active MMP-7 clearly processed RANKL into two major fragments with molecular weights of approximately 24 kDa and 12 kDa (Figure 5A). Since RANKL is sensitive to metalloproteinase-mediated cleavage, we tested other bone-relevant MMPs. Interestingly, MMP-3, which shares similar ECM and non-ECM substrates with MMP-7, was also found to cleave RANKL, while other MMPs, such as MMP-2, MMP-9, and MMP-13, did not (Figure 5A). In the presence of the broad-spectrum MMP inhibitor BB-94, neither MMP-3 nor MMP-7 processed RANKL, confirming that

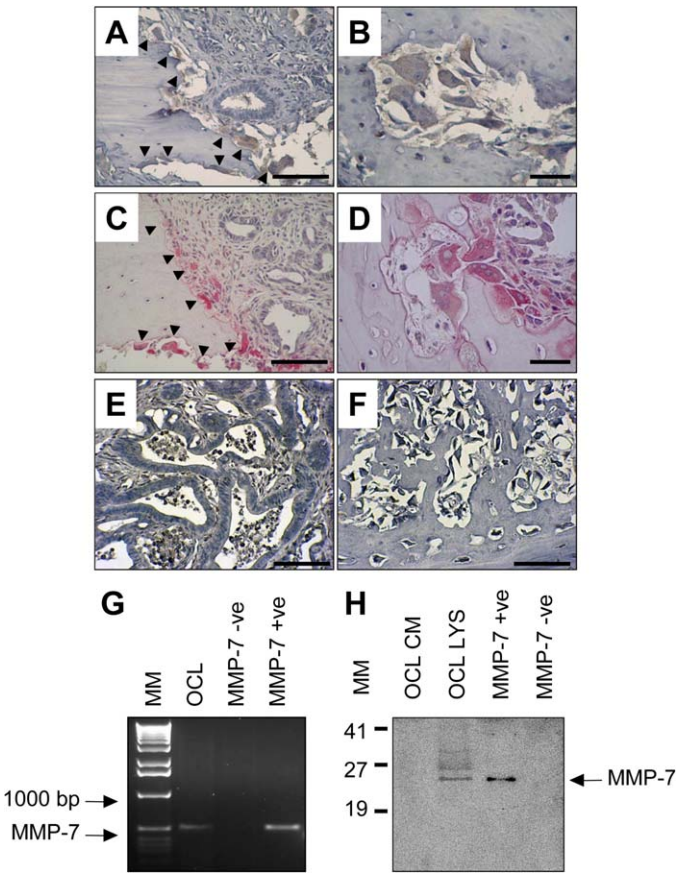

Figure 4. Localization of MMP-7 expression at the TB interface

A–B: Immunohistochemistry for MMP-7 at week 4. Osteoclasts are indicated by arrows. Scale bar = 0.05 mm (**A**) and 0.02 mm (**B**).

C–D: TRAP staining (red) as a marker for osteoclasts (arrows). Scale bar = 0.05 mm (**C**) and 0.02 mm (**D**).

E–F: MMP-7 immunohistochemistry was negative in the tumor area and areas of osteoblastic change, respectively. Scale bars = 0.05 mm.

G–H: MMP-7 was also detected in $OCL_{BCL\text{-}XL/TAG}$ (OCL) cells at the mRNA and protein levels, respectively. MM refers to the molecular weight marker in base pairs (**G**) and in kDa (**H**). Suffixes CM and LYS refer to conditioned media and lysate, respectively. Cell lines known to be positive and negative for MMP-7 were used as positive controls.

MMP-3 and MMP-7 enzymatic activity was responsible for the observed proteolysis (Figure 5B). The enzymatic activity of each MMP was confirmed by incubation with fluorescently quenched gelatin. Within 150 min, all of the MMPs tested for RANKL cleavage ability showed evidence of gelatin degradation as measured by an increase in fluorescence (Figure 5C). To determine the site of RANKL cleavage, N-terminal amino acid sequencing was performed on the major fragment generated by MMP-7 upon incubation with recombinant RANKL (Figure 5D). The sequence of this product was MEGSPLDVAQ, which corresponds to residues 146–155 in the stalk region of RANKL. The cleavage of RANKL in the stalk region suggests that MMP-7 processing results in the release of an active ligand from the cell surface (Figure 5E).

Next, we addressed if MMP-7 could access and cleave glycosylated RANKL on the cell surface. The RANKL protein expression vector was transfected into the Cos-7 cell line, which does not endogenously express RANKL (data not shown). Cell lysates showed the presence of a predicted 45 kDa glycosylated membrane-associated RANKL protein (Figure 5F, control lane, top panel). Addition of MMP-7 to the transfected cells resulted in full-length RANKL being cleaved from the cell surface and the detection of an expected 24 kDa soluble form of RANKL in the conditioned media (Figure 5F; middle panel). Similar results were also obtained for MMP-3, although the amount of soluble RANKL produced was significantly less. The addition of BB-94 completely inhibited the MMP-dependent solubilization of RANKL from the cell surface (Figure 6F). These data indicate that MMP-7 is capable of generating soluble RANKL from the surface of RANKL-expressing cells.

MMP-7-solubilized RANKL promotes osteoclast activation

Next we asked if the soluble form of RANKL generated by MMP-7 was functional. Monocyte precursors from human peripheral blood were isolated and treated with normal media (control) or media containing either MMP-7-solubilized or full-length RANKL. Histochemical analysis of TRAP and actin ring formation demonstrated relatively few mature osteoclasts in the controls compared to cells treated with MMP-7-solubilized RANKL and full-length RANKL (Figures 6A and 6C versus Figures 6B and 6D and data not shown). The numbers of mature osteoclasts in full-length RANKL- and MMP-7-cleaved RANKL-treated cells were similar, suggesting that MMP-7-solubilized RANKL was active and efficient at osteoclast activation (Figure 6E). In addition, osteoclasts activated by either full-length or MMP-7-solubilized RANKL were functional and capable of forming resorptive pits in dentin slices (Figure 6F versus Figure 6G and data not shown). MMP-7-solubilized RANKL was comparable to full-length RANKL with respect to the number of resorptive pits formed on the dentin surface (Figure 6H).

Tumor-induced osteolysis is significantly reduced in MMP-7-deficient mice

To specifically address the contribution of MMP-7 to tumor-induced osteolysis, the rat prostate tumor tissue was transplanted to the calvarias of 6-week-old immunocompromised MMP-7 wild-type and MMP-7-deficient mice. Micro-CT scanning revealed that, by week 3, there was extensive osteolysis in the calvaria of the wild-type mice, while noticeably less osteolysis was observed in the MMP-7-deficient animals (Figures 7A and 7B). Segmentation analysis of the CT data to quantitate the density of the wild-type and MMP-7-deficient mouse skulls revealed that there was significantly less bone in the wild-type calvaria, consistent with extensive osteolysis (Figure 7C). No difference was observed in the density of the calvaria from age-matched nontransplanted wild-type and MMP-7-deficient mouse skulls, suggesting that the MMP-7-deficient animals had normal bone density (data not shown). Histological analysis of the TB interface confirmed extensive osteolysis at the TB interface in wild-type mice compared to MMP-7-deficient animals (Figures 7D and 7E). Analysis of the bone destruction index indicated a 66% reduction in bone destruction in MMP-7-deficient mice compared to wild-type controls (Figure 7F).

As expected, only the osteoclasts in the wild-type mice stained positive for MMP-7 (Figures 7G and 7H). Furthermore, significantly fewer osteoclasts were observed at the TB interface in the MMP-7-deficient mice (Figure 7H). To confirm that

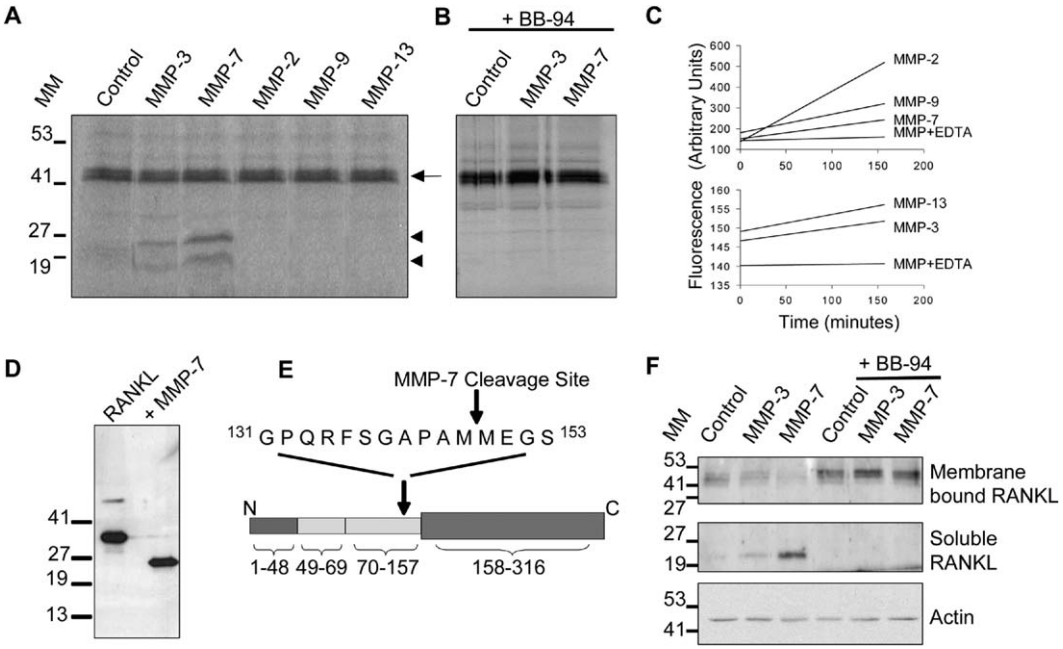

Figure 5. RANKL is cleaved by MMP-7

A: Recombinant MMP-2, -3, -7, -9, and -13 were incubated with in vitro-translated RANKL. Arrow indicates full-length RANKL. Closed arrows indicate 24 kDa and 12 kDa RANKL cleavage products.

B: RANKL was incubated with MMP-3 and MMP-7 in the presence of the broad-spectrum MMP inhibitor BB-94.

C: The activity of each of the MMPs was tested against a fluorescently quenched common substrate, gelatin.

D: Recombinant RANKL was also cleaved with recombinant MMP-7 and the cleavage products were analyzed by N-terminal amino acid sequencing.

E: MMP-7 cleavage of RANKL occurred in the stalk region at ^{145}Met-Met^{146}. Numbers 1–316 represent the amino acids in full-length RANKL (1–48, cytoplasmic region; 49–69, transmembrane region; 70–157, stalk region; and 158–316, active ligand moiety).

F: Immunoblot analysis of RANKL cleavage from the cell surface of RANKL-transfected Cos-7 cell lines in the presence or absence of the broad-spectrum MMP inhibitor BB-94 (5 μM) (top and middle panel). Actin was used to control for equal loading of the lysate samples (lower panel). MM refers to the protein molecular weight in kDa.

MMP-7 was mediating RANKL solubilization in vivo, we immunoprecipitated the soluble form of RANKL from the TB interface lysates from wild-type and MMP-7-deficient mice. Soluble RANKL was clearly detected in the TB interface lysates from the wild-type mice, while little or no soluble RANKL was detected in the MMP-7-deficient animals (Figure 7I). Soluble RANKL was not detected in the lysates of the tumor area alone from either group. These data indicate that stromal MMP-7 clearly contributes to the solubilization of RANKL at the TB interface.

Discussion

Using a model of rat prostate cancer in the bone that features both osteolytic and osteoblastic changes, we identified MMP-7 as a candidate gene involved in prostate cancer-induced bone resorption. Further investigation demonstrated that MMP-7 was secreted by osteoclasts at the TB interface, and processed RANKL to a soluble form capable of promoting osteoclast activation and bone resorption (Figure 8). The use of MMP-7-deficient mice demonstrated that MMP-7 in the tumor-bone microenvironment is an important mediator of prostate cancer-induced osteolysis.

An animal model of prostate cancer in the bone environment

To date, human prostate cancer metastasis in the bone has been difficult to mimic in animal models. In existing models of prostate carcinogenesis such as the transgenic adenocarcinoma of mouse prostate model (TRAMP) and the SV-40 probasin transgenic rat model, lymph node and pulmonary metastases are common, but the induction of bone metastases from the primary tumor site is rare (Gingrich and Greenberg, 1996; Asamoto et al., 2001). Using available prostate cancer cell lines, it has also been difficult to mimic the clinical patterns of osseous metastasis of human prostate cancer. These models include tail vein, intracardiac, or orthotopic injection of prostate cancer cell lines or the use of femoral human bone implanted into nude mice (Arguello et al., 1988; Zhang et al., 2001; Fisher et al., 2002; Nemeth et al., 1999). Our bone invasion model of rat prostate cancer requires a simple surgical technique of transplantation of rat prostate tumor tissue onto the surface of the calvaria or spinal column, ensuring that both intramembraneous and cartilaginous bone can be easily examined. The resulting tumors are moderately differentiated rat prostate adenocarcinoma with osteolytic and osteoblastic changes that are similar to the histopathological features of bone metastasis of human prostate cancer (Keller and Brown, 2004). Our model

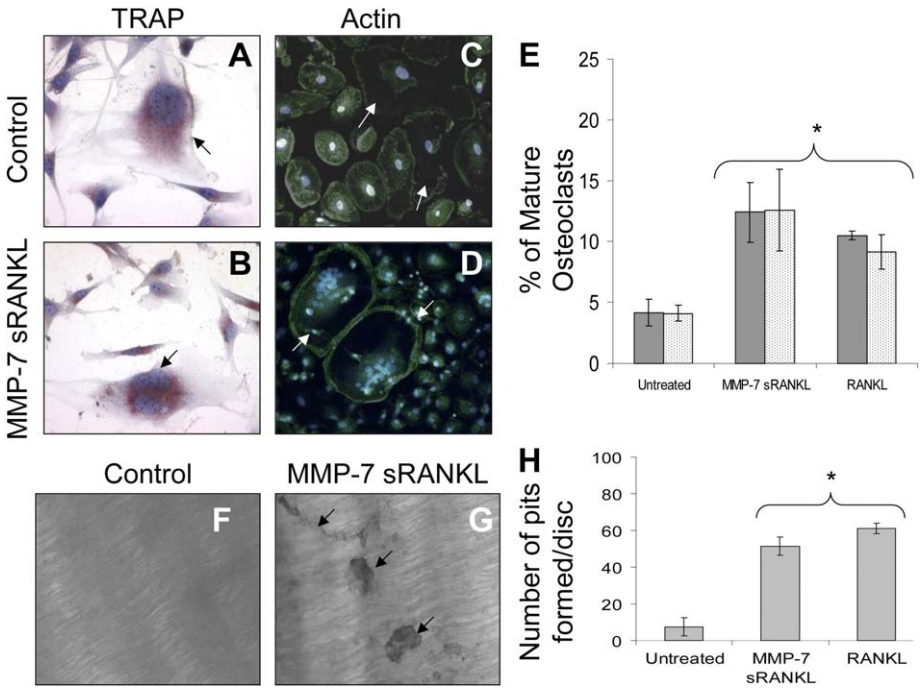

Figure 6. MMP-7-solubilized RANKL promotes osteoclast activation and bone resorption

A–B: Control cells stained positive for TRAP activity (dark brown granules) but were typically mononuclear (arrows), while MMP-7-solubilized RANKL-treated osteoclasts were active, as indicated by positive TRAP staining and multinucleation (arrows).

C–D: Actin (green) cortical rings were rarely detected in untreated control cells, while MMP-7-soluble RANKL-treated osteoclasts displayed actin cortical rings structures and multinucleation (arrows).

E: The osteoclasts determined by cytochemistry were counted and expressed as a percentage of the total number of cells. Gray and dotted bars indicate the percentage of osteoclasts as determined by TRAP and actin staining, respectively. Bars = mean ± SD.

F–G: Control and MMP-7-solubilized RANKL-treated osteoclasts were incubated on dentin slices, and the number of resorptive pits quantitated.

H: The total number of pits on each disc was counted, and the mean standard deviation of the number of pits formed is displayed. *, $p < 0.05$ ($n = 5$ for each assay).

has limitations in that it does not represent the process of human prostate-to-bone metastasis or the typical location in the bone where metastatic prostate tumors arise. However, as the model accurately reflects how human prostate cancers behave in the bone, we feel that these limitations are outweighed by the potential for defining how tumor cells can effect changes in bone matrix homeostasis. In this regard, our animal model has proved extremely useful in allowing us to identify key factors driving tumor-induced osteoblastic and osteolytic changes.

MMP-7 in the pathological bone environment

Over the past decade, it has become increasingly clear that the MMPs are exquisite regulators of cell:cell communication, and this is primarily achieved through the solubilization of non-matrix molecules such as cytokines and growth factors. For example, MMP-7 has been shown to process TNF, FasL, and E cadherin, and as a consequence of these actions, profound changes on cellular behavior have been observed (see [Lynch and Matrisian, 2002] for review). Therefore, the detection of MMP-7 and its increased expression over time at the TB interface made it an interesting target to pursue in order to better understand the biology of the prostate tumor-induced osteolysis.

The solubilization of RANKL by MMP-7 appears to be at least one mechanism by which MMP-7 mediates osteolysis in our model. The current theory is that osteoclasts become activated via the direct interaction of the immature osteoclast cell with the RANKL-expressing osteoblast (see [Mundy, 2002] for review). Therefore, one major implication for the presence of MMP-7-solubilized RANKL at the TB interface is that it allows the immature osteoclast to circumvent the requirement for direct interaction with osteoblasts. To support this argument, soluble RANKL has been detected in vivo in pathological bone-degrading diseases such as multiple myeloma (Terpos et al., 2004). Furthermore, in transgenic animals, the targeted expression of soluble RANKL in hepatocytes has been shown to cause severe osteolysis in mice (Mizuno et al., 2002).

Although RANKL expression was mainly localized to the osteoblasts in our study, previous reports have demonstrated RANKL expression in primary and bone metastatic prostate cancers (Brown et al., 2001). The expression of membrane-bound RANKL was also demonstrated by Keller and colleagues in the LnCAP prostate cancer cell line and the LnCAP-derived bone homing metastatic cell line, C4-2B (Zhang et al., 2001). Interestingly, this group also showed that these cell lines secrete a 24 kDa soluble version of RANKL which is the same size as the soluble RANKL generated by MMP-7. Furthermore, Bowden and colleagues have observed MMP-7 expression in the LnCAP prostate cancer cell line, suggesting that, at least in vitro, MMP-7 may be responsible for the secreted 24 kDa version of RANKL observed in both LnCAP and C4-2B (Klein et al., 1997). In our in vivo model, little or no MMP-7 expression was detected in the prostate tumor cells, and we clearly demonstrated the importance of stromal MMP-7 to prostate tumor-induced osteolysis by using MMP-7-deficient animals. Therefore, it appears that in the pathological bone environment, MMP-7 can be derived from both the stroma and, potentially, the prostate tumor cells, and by solubilizing RANKL, MMP-7 promotes osteoclast activation and bone resorption (Figure 8).

MMPs and RANKL solubilization

In the current study, soluble RANKL was detected in the TB interface lysates from the MMP-7-deficient animals, albeit to a much lesser extent than the wild-type controls, suggesting that other proteinases in addition to MMP-7 contribute to RANKL cleavage during tumor-induced bone destruction. MMP-3 has been shown to be expressed by osteoblasts (Breckon et al.,

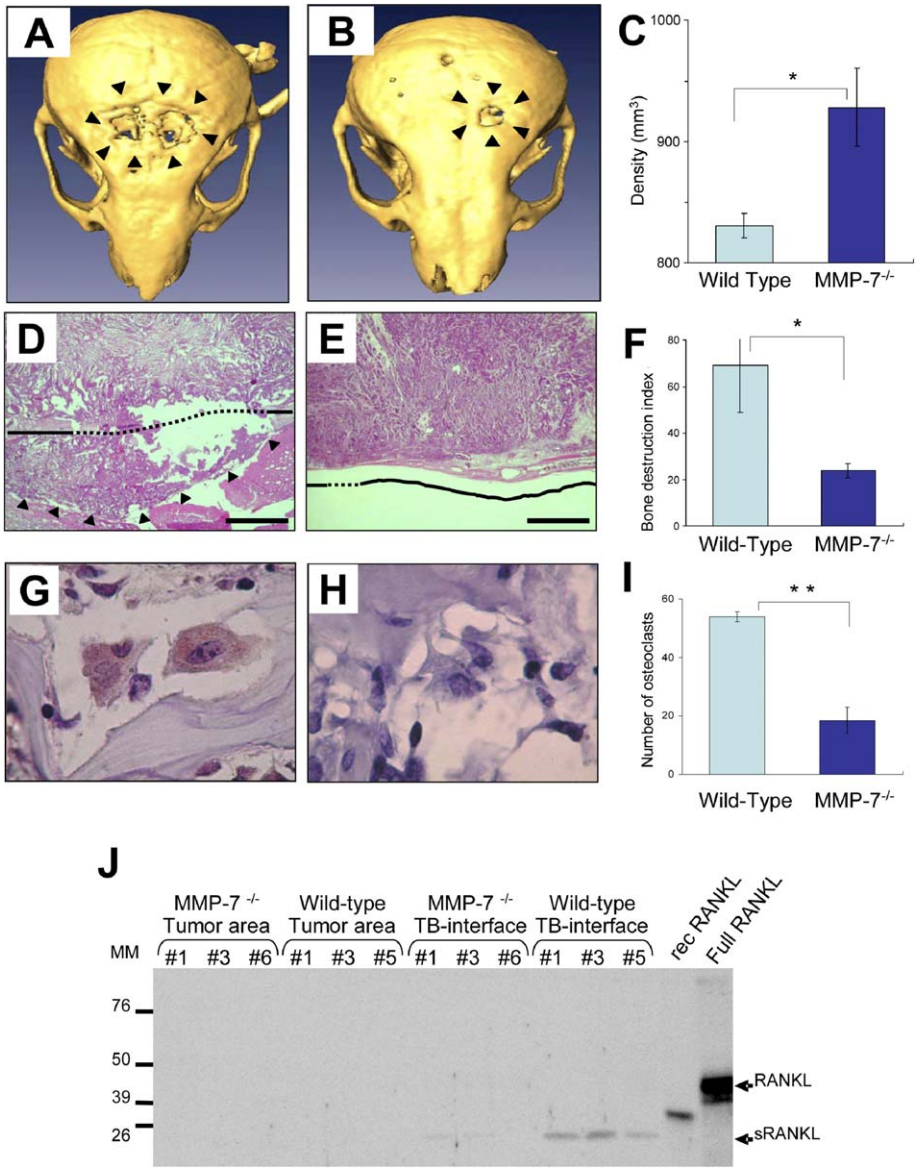

Figure 7. MMP-7-deficient animals exhibit less osteolysis and decreased shedding of RANKL

A–B: The calvaria of immunocompromised age-matched male MMP-7-deficient mice and wild-type mice were transplanted with rat prostate cancer tissue. After 3 weeks, large areas of osteolysis (arrows) were observed in the wild-type animals (**A**) compared to the MMP-7-deficient animals (**B**).

C: Quantitative segmentation analysis of the μCT scan data using Amira software demonstrated that there was significantly less bone in the MMP-7 wild-type animals (mean ± SD, 4 wild-type and 6 MMP-7 null mice; *, $p < 0.05$).

D–E: Histological analysis of H&E-stained sections from the tumors growing in the wild-type (**D**) and MMP-7-deficient animals (**E**) demonstrated that there was much less invasion of prostate tumor cells in the MMP-7-deficient animals (the dashed line represents area of resorbed calvaria, while the solid line represents the intact calvaria). Arrows in **D** represent the invading tumor cells. Scale bar is 1 mm.

F: Bone destruction index. Mean ± SD, n = 4 wild-type and n = 6 MMP-7 null. *, $p < 0.05$.

G–H: Using immunohistochemistry, MMP-7 was only detected in the wild-type osteoclasts (**G**) and not in the MMP-7-deficient osteoclasts (**H**).

I: Osteoclasts at the TB interface were counted. Mean ± SD, n = 4 wild-type and n = 6 MMP-7 null. **, $p < 0.01$.

J: Immunoprecipitation using antibodies directed toward the N terminus of RANKL demonstrated that soluble RANKL (sRANKL) was present in the TB interface lysates from the MMP-7 wild-type mice. The numbers above each lane represent the individual mouse numbers from mice in the wild-type and MMP-7-deficient groups. As positive controls, direct immunoblot analysis of full-length RANKL (full RANKL) from transfected Cos-7 lysates, which migrates at approximately 45 kDa, and recombinant RANKL (rec RANKL), which migrates at approximately 35 kDa, were added. MM refers to the molecular marker in kDa.

Error bars represent standard deviation.

1999) and is capable of cleaving RANKL (Figure 5). Therefore, the expression of MMP-3 at the TB interface may also be contributing to the cleavage of RANKL in our model. Previous in vitro reports have also demonstrated that MMP-1, MMP-14, and members of the ADAM (a disintegrin and metalloproteinase) family, ADAM-17 and ADAM-19, are capable of cleaving RANKL to a soluble form (Chesneau et al., 2003; Schlondorff et al., 2001). Although these metalloproteinases may be involved in the processing of RANKL, no in vivo evidence for a role in bone resorption currently exists. We also examined other MMPs known to have roles in the bone environment, including MMP-9 and MMP-13, as mice deficient in these enzymes have been reported as having defects in osteoclast function and bone development (Vu et al., 1998; Inada et al., 2004). However, neither MMP-9 nor MMP-13 was capable of processing RANKL to a soluble form, suggesting that they affect osteoclast activity either by the processing of extracellular matrix or through the solubilization of other nonmatrix factors.

The clinical relevance of MMP-7 in the metastatic prostate bone tumor

The identification of MMP-7 expression by osteoclasts and the elucidation of how this proteinase contributes to prostate tumor-induced osteolysis makes it an exciting therapeutic target for the treatment of this disease. A number of recent studies have shown that there is great potential for the use of MMPIs in the treatment of prostate and breast osteolytic lesions (Lee et al., 2001; Nemeth et al., 2002; Winding et al., 2002). These in vivo studies demonstrated that the administration of broad-spectrum MMPIs to animals with metastatic bone tumors not only reduced the extent of tumor-induced osteolysis, but also inhibited the growth of the tumor. However, cautionary tales exist for the use of broad-spectrum MMPIs in the clinical setting. Although for the most part, the aberrant expression of MMPs appears to contribute to tumor progression, in some instances, the increased expression of MMPs can suppress tumorigenesis and inhibit angiogenesis (see [Coussens et al.,

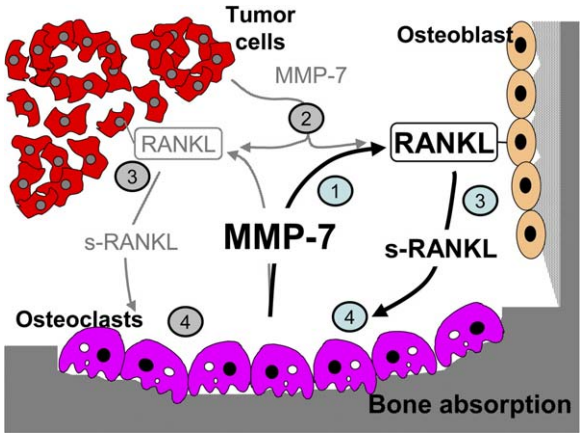

Figure 8. Role of MMP-7 in the pathological bone environment

In our model, MMP-7 is expressed by the osteoclasts (1). Previous studies have shown that MMP-7 can be expressed by prostate cancers (2). The secretion of MMP-7 results in the solubilization of RANKL being presented by the osteoblast or tumor cells in the bone microenvironment (3). Soluble RANKL is then capable of mediating the activation of osteoclasts at or near the TB interface, resulting in bone degradation (4). Blue numbers in the diagram illustrate how MMP-7-solubilized RANKL works in our model, while gray numbers represent how MMP-7 derived from the tumor cells can drive RANKL solubilization and osteoclast activation.

2002] for review). In this regard, the identification of the role of specific MMPs in tumor progression is important with respect to minimizing the potential side effects from unexpected protective functions of the MMPs.

In conclusion, we have established a model of rat prostate cancer in the bone environment that features areas of osteolytic and osteoblastic change. We used the model to identify genes that are expressed in the tumor-bone interface compared to the tumor alone. This approach identified the aberrant regulation of several genes, including cathepsin-K, an osteoclast-produced enzyme known to contribute to bone resorption, and revealed MMP-7 as another proteolytic enzyme whose expression correlated with tumor-induced osteolysis. We made the observation that MMP-7 was also produced by osteoclasts, and was a major contributor to prostate cancer-induced osteolysis. In addition, MMP-7 cleaved RANKL to a soluble active form in vitro and in vivo, establishing a mechanism for MMP-7 action in bone destruction. These results make MMP-7 an attractive therapeutic target for the control of cancer-induced bone osteolysis.

Experimental procedures

Animal models and tissue preparation

The rat prostatic carcinoma tissues used in this experiment were established from primary tumors that developed in the dorsolateral prostate of F344 rats receiving combined treatments of DMAB (3-2′ dimethyl 4-aminobiphenyl) and testosterone propionate as previously described (Kato et al., 1998). Tumors were subsequently transplanted into 6-week-old F344 male rats. Tumor growth at the implanted sites and body weight were measured weekly, and bone matrix turnover was assessed by X-ray radiograms (Shimazu, XED125M). Tumors were also implanted into 6-week-old MMP-7-deficient (n = 6) and wild-type control immunodeficient mice (n = 4). These mice were generated by breeding MMP-7-deficient mice (c57BL/6 background) to RAG-2 (recombination activation gene-2) immunodeficient mice (c57BL/6 background from Taconic) in order to generate double knockout animals. Littermates that were wild-type for MMP-7 but knockout for RAG-2 were used as controls (Wilson et al., 1997; Shinkai et al., 1992). Micro computer tomography (μCT) scanning (Concorde) and quantitation of osteolytic lesions using segmentation analysis (Amira) were performed at weeks 1, 2 and 3 posttransplantation. Animals were sacrificed at week 3 based upon μCT scan analysis. After sacrifice, the samples were divided in two with one half used for histology. The other half was separated into tumor area alone or tumor-bone interface. These samples were then flash frozen for microarray analysis or protein lysis. For histological examination and immunohistochemistry, the samples were fixed with periodate-lysine-paraformaldehyde (PLP) at 4°C for 48 hr. The tissues were then transferred into a decalcification solution (15% EDTA with glycerol [pH 7.4–7.5]) for 4 weeks and were subsequently paraffin-embedded.

Microarray analysis, real-time PCR, and RT-PCR

Calcified frozen specimens from the 4-week time point were serially sectioned in 10 μm thick slices, and at least ten slides per rat were microdissected, with careful separation of the tumor bone interface (TB interface) and the tumor areas. Equal amounts of total RNA were extracted from each microdissected population, pooled, and amplified using Atlas SMART probe amplification kit (Clontech). Probe synthesis of cDNA arrays, poly(A)$^+$ RNA enrichment, and ^{32}P labeling were performed according to the manufacturer's instructions (SMART PCR cDNA synthesis Kit; Clontech). An Atlas Rat 1.2 Array (Clontech) was used for comparing gene expression profiles between TB interface and the tumor areas. Signals were detected and analyzed by image analyzer (FLA-3000G; Fujifilm) with Array Gauge software (Fujifilm).

Real-time quantitative PCR was performed on cDNA isolated from each area. 2 μl of cDNA samples was added to 20 μl reactions using FastStart DNA Master SYBR Green I and a Light Cycler apparatus (Roche Diagnostics). Primers used were: for *Apo-D*, 5′-GTG-CGA-AAC-AAG-GAG-CTG-CGC-3′ and 5′-TGG-CGA-TGT-CGA-TGT-CAT-TAG-A-3′; for *MMP-7*, 5′-GTG-GCA-TTC-CAG-AAC-TGT-CAC-C-3′ and 5′-CCT-AGA-GTG-TTT-CCT-GGC-CCA-T-3′; for *cathepsin K*, 5′-CAG-GAA-CAC-AAA-TGC-ATC-ATG-G-3′ and 5′-GCT-GTT-TCT-GTC-CCA-AAT-TCC-A-3′; for *AQP-8*, 5′-GAA-CTG-CTC-TTC-CTC-TTG-CGA-A-3′ and 5′-ACC-GTG-AAT-GTG-ATC-TCC-TTG-G-3′. Initial denaturation at 95°C for 10 min was followed by 40 cycles with denaturation at 95°C for 15 s, annealing at 60°C for 5 s, and elongation at 72°C for 30 s. The fluorescence intensity of the double-strand-specific SYBR Green I, reflecting the amount of formed PCR product, was monitored at the end of each elongation step. *GAPDH* mRNA levels were used to normalize the sample cDNA content. For reverse transcription PCR (RT-PCR) analysis of *MMP-7* expression in vitro, the following primers were used after a standard reverse transcription reaction for cDNA generation: *MMP-7* sense 5′-TGG-AGT-GCC-AGA-TGT-TTG-CAG-3′, and anti-sense, 3′-TTT-CCA-TAT-AGC-TTC-TGA-ATG-CCT-5′. PCR conditions for *MMP-7*: 1 cycle of 95°C for 5 min, and 35 cycles of 95°C for 60 s, 57°C (MMP-7) for 60 s, and 72°C for 2 min. The expected base pair (bp) product for MMP-7 was 519 bp.

Immunohistochemistry and cytochemistry

For the in vivo detection of MMP-7 and RANKL, sections were rehydrated through a series of ethanols, and endogenous peroxidases were quenched in 0.6% H_2O_2 in methanol for 15 min. For antigen retrieval, the sections were brought to boiling in 0.1 M citrate buffer (pH 6.0). Using standard blocking criteria, the sections were blocked for 1 hr at room temperature. MMP-7 or RANKL (Shattuck-Brandt et al., 1999; Santa Cruz, sc-7628) antibody were diluted (1:100) in blocking solution, and the sections were incubated overnight at 4°C. After washing, the slides were incubated with biotinylated species-specific secondary antibodies diluted 1:500 for 30 min (Vector Laboratories), washed, and then incubated with avidin-peroxidase complex (ABC, Vector Laboratories) for 30 min. The slides were developed using diaminobenzidine tetrahydrochloride (DAB) (Sigma) substrate. The sections were counterstained with hematoxylin, dehydrated, and permanently mounted. Species-specific IgG isotype were added in lieu of primary antibody as controls, and these sections demonstrated no detectable staining.

TRAP assays were performed to detect activated osteoclasts in vitro and in vivo according to manufacturer's instructions (Sigma). In addition, osteo-

clasts were also identified in vitro by fluorescent actin ring staining using Oregon Green 488 phalloidin (1:1,000, Molecular Probes) as per manufacturer's instructions.

Immunoblotting and immunoprecipitation

Conditioned media and cell or tumor and tumor-bone lysates were collected using standard procedures. All samples were carefully measured for total protein content using a BCA assay (Pierce) to ensure equal loading. For immunoprecipitation (IP), 2 mg of tissue lysates was precleared with protein sepharose-G (Pharmacia) and then incubated overnight at 4°C with 1 μg of an antibody that recognized the N terminus of RANKL (sc-7268, Santa Cruz). Soluble RANKL was then precipitated by the addition of protein sepharose G for 1 hr at 4°C. Loading buffer was added and the samples were boiled prior to being resolved on 15% SDS-PAGE gels and then transferred onto nitrocellulose. The blots were blocked using standard blocking reagents and then incubated in primary antibody for the N terminus of RANKL (diluted 1: 1,000 in blocking solution; Alexis Biochemicals) or MMP-7 (1: 10 in blocking solution [Shattuck-Brandt et al., 1999]) overnight at 4°C with shaking. The blots were washed and incubated for 1 hr with a biotinylated anti-species secondary antibody (1:10,000; Vector Laboratories). After washing, the blots were incubated for 30 min with streptavidin-horse radish peroxidase (1:15,000; Jackson Immunoresearch). Bands were detected using enhanced chemiluminescence (ECL) and exposure to light-sensitive film. As a control for equal loading of the cell lysates, immunoblots for actin (sc-1615, Santa Cruz) were also performed.

MMP cleavage of RANKL and identification of cleavage site

Total RNA was isolated from murine mammary glands and *RANKL* cDNA was generated using standard RT protocols. Full-length RANKL was amplified using the following primers: sense, 5′-CGC-GCT-CGA-GAT-GCG-CCG GGC-CAG-3′, and anti-sense, 3′-GCG-CAA-GCT-TAA-GTT-CCA-CGA-AAT-GAG-TCT-CAG-5′. The PCR conditions were as follows: 1 cycle of 95°C for 5 min, and 35 cycles of 95°C for 60 s, 60°C for 60 s, and 72°C for 4 min, to give an expected product of approximately 975 base pairs. *RANKL* cDNA was then inserted into the protein expression vector pcDNA3.1/Zeo$^-$ (Invitrogen Life Technologies). Using ^{35}S labeled methionine, the RANKL protein was translated in vitro using a commercially available kit (TnT T7 transcription/translation system, Promega) according to the manufacturer's instructions. Subsequent full-length RANKL protein was incubated for 6 hr at 37°C with either MMP-3, MMP-7, MMP-2, MMP-9, or MMP-13 (Oncogene/Calbiochem) in the following reactions: 10 μl of full-length RANKL in vitro translated product with 100 ng of each active MMP to be tested, and brought to a final volume in 50 μl of buffer (0.15 M NaCl, 50 mM Tris-HCl [pH 7.6], 5 mM CaCl2). Reactions were stopped with the addition of 10 mM EDTA. For analysis of cleavage products, samples were resolved using a 15% SDS-PAGE gel. The gels were then dried and imaged with autoradiography film. For MMP inhibition, BB-94 (British Biotech) at a final concentration of 5 μM was added to the reactions prior to incubation. The functional activity of the MMPs was confirmed by adding 100 ng of enzyme to 0.8 μg of DQ-gelatin substrate (Molecular Probes) in a final volume of 80 μl of reaction buffer (50 mM Tricine [pH 7.4], 0.2 M NaCl, 10 mM $CaCl_2$, 50 μM $ZnSO_4$ and 0.005% Brij 35) and assaying for the increase in fluorescence (Ex 485 nm; Em 530 nm) over 150 min. EDTA (10 mM) was also added to separate reactions to demonstrate that the increases in fluorescence were due to MMP activity. For identification of the RANKL cleavage site, 2 μg of recombinant RANKL (R&D Systems) was incubated overnight at 37°C with 100 ng of active of MMP-7. The MMP cleavage products were resolved using 15% SDS-PAGE gels, transferred to polyvinyl difluoride (PVDF) membranes, and stained with 0.025% Coomassie in 40% MeOH. The 24 kDaA band was excised from the PVDF and submitted for N-terminal amino acid sequencing to Proseq Inc.

Cell culture and transient transfection assays

$OCL_{BCL\text{-}XL\ TAG}$ cells were a kind gift from Dr. David G. Roodman, and Cos-7 cells were obtained from the ATCC. Conditioned media was obtained by culturing the $OCL_{BCL\text{-}XL\ TAG}$ cells for 48 hr in serum free media. For transient transfections, Cos-7 cells were transfected with 1 μg of the RANKL expression vector using Superfect reagent (Qiagen) as per manufacturer's instructions. For cleavage of RANKL by MMPs, Cos-7 cells were incubated in serum-free media containing active MMP-3 or MMP-7 at a concentration of 100 ng/ml for 24 hr. For MMP inhibition studies, the broad-spectrum MMP inhibitor BB-94 was added to the cells at a concentration of 5 μM daily. After incubation, conditioned media was removed, and the cells were lysed using a membrane lysis buffer (0.5% NP-40, 50 mM Tris-HCl [pH 7.5], 100 mM NaCl) with protease and phosphatase inhibitors. Equal amounts of protein from the cell lysates and conditioned media were loaded for immunoblotting.

Osteoclast activity and functional assays

Using standard procedures, monocytes were collected from human peripheral blood, and 5×10^5 cells were incubated in either 8-well chamber slides or 96-well plates containing dentin discs (Alpco) for one hour. Adherent cells were washed extensively, then treated with α-MEM media containing 10% FBS alone (control) or containing RANKL at 50 ng/ml or MMP-7-cleaved RANKL at 50 ng/ml. Cells were treated every 2 days for 3 weeks and subsequently analyzed for osteoclast formation. For the osteoclast activity assay, the numbers of osteoclasts in three random fields at 10× magnification from multiple replicate experiments were photographed, and fully mature multinucleated TRAP-positive or actin ring-positive osteoclasts were counted in each test and control experiment. For osteoclast functionality assays, dentin discs were removed from culture and sonicated for 2 min in 5 ml of 0.25 M ammonium hydroxide to remove cells. The discs were then stained for 5 min (0.05% toluidine blue in 40% MeOH) and air-dried. The total number of pits formed per disc was counted using reflective light microscopy.

Statistical analysis

For in vivo data, statistical analysis was performed using the Kruskal-Wallis and Bonferroni/Dunn multiple comparison tests. In vitro data are presented as mean ± standard deviation (SD). In vitro, statistical significance was analyzed using a two-tailed student's t test. A value of $p < 0.05$ was considered significant.

Acknowledgments

This work was supported by a grant from the NIH (R01 84360 to LMM), Grants-in-Aid for Cancer Research from the Ministry of Education, Culture, Sports, Science, and Technology and the Ministry of Health, Labor, and Welfare, Japan, a Grant-in-aid from the Ministry of Health, Labor and Welfare for the Second-Term Comprehensive 10-Year Strategy for Cancer Control, Japan, and a grant from the Society for Promotion of Pathology of Nagoya, Japan. C.C.L. is supported by grant PDF02-1394 awarded by the Susan G. Komen Breast Cancer Foundation. We also thank Oliver McIntyre and Lisa McCawley for their valuable critique.

Received: October 1, 2004
Revised: February 28, 2005
Accepted: April 5, 2005
Published: May 16, 2005

References

American Cancer Society. (2004). Cancer Facts and Figures 2004. http://www.acs.org.

Arguello, F., Baggs, R.B., and Frantz, C.N. (1988). A murine model of experimental metastasis to bone and bone marrow. Cancer Res. *48*, 6876–6881.

Asamoto, M., Hokaiwado, N., Cho, Y.M., Takahashi, S., Ikeda, Y., Imaida, K., and Shirai, T. (2001). Prostate carcinomas developing in transgenic rats with SV40 T antigen expression under probasin promoter control are strictly androgen dependent. Cancer Res. *61*, 4693–4700.

Breckon, J.J., Papaioannou, S., Kon, L.W., Tumber, A., Hembry, R.M., Murphy, G., Reynolds, J.J., and Meikle, M.C. (1999). Stromelysin (MMP-3) synthesis is up-regulated in estrogen-deficient mouse osteoblasts in vivo and in vitro. J. Bone Miner. Res. *14*, 1880–1890.

Brown, J.M., Corey, E., Lee, Z.D., True, L.D., Yun, T.J., Tondravi, M., and Vessella, R.L. (2001). Osteoprotegerin and rank ligand expression in prostate cancer. Urology *57*, 611–616.

Chay, C.H., Cooper, C.C., Hellerstedt, B.A., and Pienta, K.J. (2002). Antimetastatic drugs in prostate cancer. Clin. Prostate Cancer *1*, 14–19.

Chesneau, V., Becherer, J.D., Zheng, Y., Erdjument-Bromage, H., Tempst, P., and Blobel, C.P. (2003). Catalytic properties of ADAM19. J. Biol. Chem. *278*, 22331–22340.

Corey, E., Quinn, J.E., Bladou, F., Brown, L.G., Roudier, M.P., Brown, J.M., Buhler, K.R., and Vessella, R.L. (2002). Establishment and characterization of osseous prostate cancer models: Intra-tibial injection of human prostate cancer cells. Prostate *52*, 20–33.

Coussens, L.M., Fingleton, B., and Matrisian, L.M. (2002). Matrix metalloproteinase inhibitors and cancer: Trials and tribulations. Science *295*, 2387–2392.

Delaisse, J.M., Andersen, T.L., Engsig, M.T., Henriksen, K., Troen, T., and Blavier, L. (2003). Matrix metalloproteinases (MMP) and cathepsin K contribute differently to osteoclastic activities. Microsc. Res. Tech. *61*, 504–513.

Fisher, J.L., Schmitt, J.F., Howard, M.L., Mackie, P.S., Choong, P.F., and Risbridger, G.P. (2002). An in vivo model of prostate carcinoma growth and invasion in bone. Cell Tissue Res. *307*, 337–345.

Gingrich, J.R., and Greenberg, N.M. (1996). A transgenic mouse prostate cancer model. Toxicol. Pathol. *24*, 502–504.

Gowen, M., Lazner, F., Dodds, R., Kapadia, R., Feild, J., Tavaria, M., Bertoncello, I., Drake, F., Zavarselk, S., Tellis, I., et al. (1999). Cathepsin K knockout mice develop osteopetrosis due to a deficit in matrix degradation but not demineralization. J. Bone Miner. Res. *14*, 1654–1663.

Hentunen, T.A., Jackson, S.H., Chung, H., Reddy, S.V., Lorenzo, J., Choi, S.J., and Roodman, G.D. (1999). Characterization of immortalized osteoclast precursors developed from mice transgenic for both bcl-X(L) and simian virus 40 large T antigen. Endocrinology *140*, 2954–2961.

Inada, M., Wang, Y., Byrne, M.H., Rahman, M.U., Miyaura, C., Lopez-Otin, C., and Krane, S.M. (2004). Critical roles for collagenase-3 (Mmp13) in development of growth plate cartilage and in endochondral ossification. Proc. Natl. Acad. Sci. USA *101*, 17192–17197.

Kato, K., Takahashi, S., Mori, S., Futakuchi, M., Cui, L., Ito, N., and Shirai, T. (1998). Establishment of transplantable rat prostate carcinomas from primary lesions induced by *3*, 2′-dimethyl-4-aminobiphenyl and testosterone. J. Toxicol. Pathol. *11*, 27–32.

Keller, E.T., and Brown, J. (2004). Prostate cancer bone metastases promote both osteolytic and osteoblastic activity. J. Cell. Biochem. *91*, 718–729.

Klein, R.D., Borchers, A.H., Sundareshan, P., Bougelet, C., Berkman, M.R., Nagle, R.B., and Bowden, G.T. (1997). Interleukin-1-beta secreted from monocytic cells induces the expression of matrilysin in the prostatic cell line Incap. J. Biol. Chem. *272*, 14188–14192.

Koyama, Y., Yamamoto, T., Kondo, D., Funaki, H., Yaoita, E., Kawasaki, K., Sato, N., Hatakeyama, K., and Kihara, I. (1997). Molecular cloning of a new aquaporin from rat pancreas and liver. J. Biol. Chem. *272*, 30329–30333.

Lee, J., Weber, M., Mejia, S., Bone, E., Watson, P., and Orr, W. (2001). A matrix metalloproteinase inhibitor, batimastat, retards the development of osteolytic bone metastases by MDA-MB-231 human breast cancer cells in Balb C nu/nu mice. Eur. J. Cancer *37*, 106–113.

Lynch, C.C., and Matrisian, L.M. (2002). Matrix metalloproteinases in tumor-host cell communication. Differentiation *70*, 561–573.

Mizuno, A., Kanno, T., Hoshi, M., Shibata, O., Yano, K., Fujise, N., Kinosaki, M., Yamaguchi, K., Tsuda, E., Murakami, A., et al. (2002). Transgenic mice overexpressing soluble osteoclast differentiation factor (sODF) exhibit severe osteoporosis. J. Bone Miner. Metab. *20*, 337–344.

Mundy, G.R. (2002). Metastasis to bone: Causes, consequences and therapeutic opportunities. Nat. Rev. Cancer *2*, 584–593.

Nakashima, T., Kobayashi, Y., Yamasaki, S., Kawakami, A., Eguchi, K., Sasaki, H., and Sakai, H. (2000). Protein expression and functional difference of membrane-bound and soluble receptor activator of NF-kappaB ligand: Modulation of the expression by osteotropic factors and cytokines. Biochem. Biophys. Res. Commun. *275*, 768–775.

Nemeth, J.A., Harb, J.F., Barroso, U., Jr., He, Z., Grignon, D.J., and Cher, M.L. (1999). Severe combined immunodeficient-hu model of human prostate cancer metastasis to human bone. Cancer Res. *59*, 1987–1993.

Nemeth, J.A., Yousif, R., Herzog, M., Che, M., Upadhyay, J., Shekarriz, B., Bhagat, S., Mullins, C., Fridman, R., and Cher, M.L. (2002). Matrix metalloproteinase activity, bone matrix turnover, and tumor cell proliferation in prostate cancer bone metastasis. J. Natl. Cancer Inst. *94*, 17–25.

Rassart, E., Bedirian, A., Do, C.S., Guinard, O., Sirois, J., Terrisse, L., and Milne, R. (2000). Apolipoprotein D. Biochim. Biophys. Acta *1482*, 185–198.

Schlondorff, J., Lum, L., and Blobel, C.P. (2001). Biochemical and pharmacological criteria define two shedding activities for TRANCE/OPGL that are distinct from the tumor necrosis factor alpha convertase. J. Biol. Chem. *276*, 14665–14674.

Shattuck-Brandt, R.L., Lamps, L.W., Heppner Goss, K.J., DuBois, R.N., and Matrisian, L.M. (1999). Matrilysin and cyclooxygenase-2 are differentially expressed in intestinal and colorectal neoplasms. Mol. Carcinog. *24*, 177–187.

Shevrin, D.H., Gorny, K.I., and Kukreja, S.C. (1989). Patterns of metastasis by the human prostate cancer cell line PC-3 in athymic nude mice. Prostate *15*, 187–194.

Shinkai, Y., Rathbun, G., Lam, K.P., Oltz, E.M., Stewart, V., Mendelsohn, M., Charron, J., Datta, M., Young, F., and Stall, A.M. (1992). RAG-2-deficient mice lack mature lymphocytes owing to inability to initiate V(D)J rearrangement. Cell *68*, 855–867.

Simonet, W.S., Lacey, D.L., Dunstan, C.R., Kelley, M., Chang, M.S., Luthy, R., Nguyen, H.Q., Wooden, S., Bennett, L., Boone, T., et al. (1997). Osteoprotegerin: A novel secreted protein involved in the regulation of bone density. Cell *89*, 309–319.

Terpos, E., Politou, M., Szydlo, R., Nadal, E., Avery, S., Olavarria, E., Kanfer, E., Goldman, J.M., Apperley, J.F., and Rahemtulla, A. (2004). Autologous stem cell transplantation normalizes abnormal bone remodeling and sRANKL/osteoprotegerin ratio in patients with multiple myeloma. Leukemia *18*, 1420–1426.

Vu, T.H., Shipley, J.M., Bergers, G., Berger, J.E., Helms, J.A., Hanahan, D., Shapiro, S.D., Senior, R.M., and Werb, Z. (1998). MMP-9/Gelatinase B is a key regulator of growth plate angiogenesis and apoptosis of hypertrophic chondrocytes. Cell *93*, 411–422.

Wilson, C.L., Heppner, K.J., Labosky, P.A., Hogan, B.L.M., and Matrisian, L.M. (1997). Intestinal tumorigenesis is suppressed in mice lacking the metalloproteinase matrilysin. Proc. Natl. Acad. Sci. USA *94*, 1402–1407.

Winding, B., NicAmhlaoibh, R., Misander, H., Hoegh-Andersen, P., Andersen, T.L., Holst-Hansen, C., Heegaard, A.M., Foged, N.T., Brunner, N., and Delaisse, J.M. (2002). Synthetic matrix metalloproteinase inhibitors inhibit growth of established breast cancer osteolytic lesions and prolong survival in mice. Clin. Cancer Res. *8*, 1932–1939.

Zhang, J., Dai, J., Qi, Y., Lin, D.L., Smith, P., Strayhorn, C., Mizokami, A., Fu, Z., Westman, J., and Keller, E.T. (2001). Osteoprotegerin inhibits prostate cancer-induced osteoclastogenesis and prevents prostate tumor growth in the bone. J. Clin. Invest. *107*, 1235–1244.

Zhau, H.E., Li, C.L., and Chung, L.W. (2000). Establishment of human prostate carcinoma skeletal metastasis models. Cancer *88*, 2995–3001.